On the effects of opposed flow conditions on non-buoyant flames spreading over polyethylene-coated wires - Part II: soot oxidation quenching and smoke release

A. Guibaud[a,*], J.M. Citerne[a], J.-L. Consalvi[b], G. Legros[a,c]

[a]*Institut Jean Le Rond d'Alembert/UMR CNRS 7190, Sorbonne Université, Paris F-75005, France*
[b]*IUSTI/UMR CNRS 7343, Aix-Marseille Université, 5 rue E. Fermi, 13453 Marseille Cedex 13, France*
[c]*ICARE/CNRS, 1C av. de la Recherche Scientifique, 45071 Orléans Cedex 1, France*

Abstract

Smoke release in the limited volume of a spaceship poses a major threat to the life of astronauts in long range exploration missions. If the absence of buoyant flows fundamentally affects combustion mechanisms, the possibility of atmospheric design in spacecraft environment provides a new leverage, not usually available on Earth. Investigating a non-buoyant flame spreading over the polyethylene coating of an electrical wire in an opposed laminar flow, the previous paper highlighted how flow conditions, namely oxygen content, flow velocity, and ambient pressure, affected spread rate and soot formation rate. The implementation of the Broadband Modulated Absorption/Emission (B-MAE) technique provided mappings of soot temperature and volume fraction in the spreading flames during parabolic flights. In this second paper, the

*Corresponding author:
Email address: augustin.guibaud@sorbonne-universite.fr (A. Guibaud)

Preprint submitted to Proceedings of the Combustion Institute *August 13, 2020*

link between these microscopic observations and new macroscopic findings regarding the influence of flow conditions on the smoke production of a flame in the same configuration is presented. Taking into account other requirements of space exploration, atmospheric conditions below normoxic values present a clear interest from a fire safety perspective. In the process, a threshold temperature at which soot oxidation reactions are frozen is identified. The value of 1400 K brought forward conforms with past measurements performed at normal gravity, while discrepancies with previous microgravity measurements are addressed. Given the broad capability of human lungs to adapt to various conditions, the overall mapping of smoke production as a function of flow conditions is a valuable tool for atmospheric design considerations.
Keywords:
Microgravity, smoke, quenching, soot, optical diagnostic, temperature

Nomenclature

C	Constant of proportionality (-)
f_s	Soot volume fraction (-)
F_s	Radially-integrated soot volume fraction f_s (m^2)
g_0	Gravitational acceleration ($m.s^{-2}$)
L_s	Characteristic soot production length (m)
$\dot{m}_F$	Pyrolysis mass flow rate ($kg.s^{-1}$)
P	Pressure (kPa)
r	Radial coordinate (m)
S	Stoichiometric Oxidizer/fuel mass ratio (-)
$t_{res,s}$	Soot residence time (s)
T	Temperature (K)
u_∞	Free stream velocity ($m.s^{-1}$)
u_p	Spread rate ($m.s^{-1}$)
$x_{O_2,\infty}$	Free stream oxygen mole fraction (-)
z	Streamwise coordinate (m)
$\dot{\omega}'''_{SP}$	Soot production rate ($kg.m^{-3}.s^{-1}$)

1. Introduction

Improvement in fire safety is among the top priorities for upcoming long range space exploration missions [1], given that present equipment and procedures implemented in fire prevention, detection, and mitigation rely heavily on the ability to send emergency supply from the Earth. If technological developments in the past 60 years have drastically reduced the amount of potential fuel aboard spacecraft, there is an irreplaceable amount of material that exhibit flaming tendency but are nonetheless found onboard given their vital features. Such is the case of polyethylene, used for radiation shielding [2], lithium perchlorate found in oxygen generators [3], or more basic equipment like paper, towels, food, magazines, and souvenirs, which are required for the comforts of living during long missions [4]. As such, accidental fires must be investigated as possible scenarios.

Past fire incidents in weightlessness highlight a shocking proportion of smoke mitigation issues [5]. Given the rapid increase in concentration of lethal pollutants in the enclosed environment of a spacecraft, the threat to the life of the astronauts is amplified. In addition, the psychological stress that results from a rapid visual impairment can undermine the intervention of well-trained astronauts [6], and potentially jeopardize the mission [7]. Since smoke tests such as ASTM D2843 [8] are systematically conducted in ground-based facilities for any material launched in orbit or beyond, it must be acknowledged that present standards fail to predict how the absence of buoyant flows affects the tendency of a flame to release smoke.

The underlying question of the transition for a laminar diffusion flame from a closed-tip configuration that does not emit smoke to an open-tip configuration that releases unburnt intermediate species in the surrounding atmosphere has been systematically investigated at normal gravity for decades [9–17]. Both fuel and oxidizer properties play a role in this transition, which means that both fuel and atmosphere should be adjusted in a spacecraft to tackle smoke emission efficiently with a naive approach. Experiments performed in various microgravity facilities have evidenced the impact of fuel and oxidizer flows on smoke-point transition over burners. Because of substantial changes in flame structure, with increased residence time in a buoyancy-free environment, unusual properties to generate smoke are reported and stress that non-buoyant flames emit smoke more readily than buoyant flames [18–20]. However, these gas-phase experiments do not take into account the modifications in flame spread rate also recorded in this unusual environment [21, 22]. As such, a holistic study of the impact of flow conditions on smoke emission in a spreading situation is required to provide thorough atmospheric recommendations within a fire safety perspective.

Atmospheric properties in a spacecraft are limited by the ability of the human body to adapt to environments of different oxygen content and pressure. The high permanent settlements on Earth provide insights on how human physiology acclimates to low pressure levels at constant oxygen content. For people living at moderate altitude (<2500 m), the level of oxygen in the arterial blood does not markedly change from that recorded at sea-level conditions [23]. Over 2500 m, where the ambient pressure is about 75 kPa, high-altitude adaptation is necessary to cope with hypoxic exposure [24]. As altitude increases, the human body is more likely to develop maladaptive features known as chronic mountain sickness (CMS). As an extreme example of adaptation, highlanders from la Riconanda, Peru, live at 5100 m above sea level where they experience a daily pressure of about 54 kPa. Indeed, a significant proportion of inhabitants seem to have developed CMS [25], but this provides a qualitative lower boundary to the range of conditions to which the body can adapt without any medication.

The overall stability of the oxygen level around the globe limits the analysis of acclimatization to low oxygen content [26], but concerns over oxygen depletion in mine shafts have driven past research in that field [27]. Keeping pressure at 101.3 kPa, a drop in oxygen content from 21% down to 19% has limited effect on the body. At 18% oxygen content, a slight increase in breathing effort together with a slight augmentation in heart rate is reported at rest. This difficulty to breath intensifies until 15%, while physical and intellectual performances are reduced without awareness. Below 15%, physical, emotional, and intellectual damages are reported, starting with emotional upset, impaired judgement, and faulty coordination. The situation worsens at lower oxygen contents, until convulsions and subsequent death occur at 10%. These results should be considered with caution in the context of long-duration spaceflight, as most experiments in oxygen-depleted environment were performed over a relatively short period of time.

The human body can also adapt to oxygen content higher than 21%, provided that the pressure is reduced [28]. Because this trade-off between oxygen content and pressure allows to reduce the pressure difference in space environment while keeping the oxygen partial pressure constant, the corresponding normoxic curve has regularly been put forward as a baseline for space exploration atmosphere [29]. Fire safety improvements in moderate hypoxic conditions should thus be discussed, since working at low oxygen content and low pressure naturally increases fire safety [30]. Atmospheric design can then consider fire safety strategies in this context once the role of pressure and oxygen content on a flame spreading in weightlessness is well documented. Given the specifics of past incidents, the mechanisms behind the role of atmospheric conditions on smoke production need to be discriminated.

Part I [5] did investigate the local effects of flow conditions on spread rate and soot production in a flame spreading over cylindrical samples in parabolic flight experiments. Capitalizing on these results, this paper makes the connection between the microscopic observation and their macroscopic consequences. Starting with a systematic mapping of the influence of flow conditions on smoke emission by the aforementioned spreading flame, this study then separately investigates the role of oxygen content, pressure, and flow velocity on the local extinction of soot oxidation reactions to document the transitions observed. Contrasting broader fire safety results with other space travel issues likely to influence atmospheric design, a tentative set of atmospheric conditions is brought forward. In addition, soot volume fraction and temperature mappings enabled by the Broadband Modulated Absorption/Emission technique provide valuable insights regarding the temperature at which soot oxidation reactions are frozen, independently of the flow conditions.

2. Macroscopic observation and related issues

Experiments conducted in parabolic flights, following a protocol described in Ref. [5] and briefly recalled in Section 3, have led to observations that highlight the impact of pressure, flow velocity, and oxygen content on the existence of a smoking plume at the trailing edge of spreading flames. Set into a nitrogen-diluted air stream flowing parallel to the sample's axis, cylindrical samples of polyethylene coated wires were ignited in an opposed flow configuration. These wires consisted of a 0.5 mm in diameter nickel-chrome core coated with a 0.3 mm thick low-density polyethylene (LDPE) layer. For a set value of free stream oxygen content, velocity, and pressure, the tendency of smoke to exit at the flame trailing edge was reported. A backlight located behind the flame evidenced this transition as the flame spreads at a steady rate using a 3-CCD camera. Oxygen content, $x_{O_2,\infty}$, varied between 18% and 21% in volume, free oxidizer stream velocity, u_∞, ranged from 100 mm.s^{-1} to 200 mm.s^{-1}, and pressure, P, was comprised between levels of 70.9 kPa and 141.8 kPa. Figure 1 highlights the frontier between non-smoking conditions, on the lower left of the plot, and smoking conditions, on the upper right, for varying pressure and oxygen content, at three different free stream velocities. The smoke point transition occurs as pressure or oxygen content is increased. However, this transition seems almost independent of free stream velocity, given the experimental uncertainties. In this spreading flame configuration, the cause of the transition can be different in nature: as Part I stressed, the spread rate varies with oxygen content while it is marginally affected by pressure over the range of flow conditions considered. Consequently, the mechanism driving the transition observed as oxygen content is increased may differ from that involved when pressure is increased, other flow parameters being set. Further detailing of the mechanism driving the smoke point transition for each flow parameter variation is thus required. In the following, experimental investigations conducted in parabolic flights document the smoke point transition with respect to oxidizer flow rate, oxygen content, and pressure variations.

These flow conditions are known to influence other features of combustion. Using the same wire samples in the same configuration, oxygen content as a function of pressure at the flammability limit has been reported by Masashi et al. at a flow velocity of 100 $mm.s^{-1}$ [31]. Along this curve, pressure decreases from $P = 150$ kPa at $x_{O_2,\infty} = 0.15$ to $P = 50$ kPa at $x_{O_2,\infty} = 0.17$. The flammability limit is thus less sensitive to pressure than the smoke point transition at the same flow velocity. The different ambient flow dependencies highlight the distinctive mechanisms at stake. The low flow velocity flammability limit belongs to the quenching branch of the extinction boundary identified by Olson et al. [32]. In such a situation, the increased flame standoff distance lowers the rate of heat feedback from the flame to the fuel surface, while the rate of heat losses from the fuel surface remains constant. The burning rate is consequently weakened, and so is the flame temperature until kinetic extinction happens. The smoke point transition investigated here is rather different. Large amounts of soot can be formed in the hot fuel-rich region of a diffusion flame away from the extinction limit. Locally, the associated soot radiative heat losses lower the temperature. If the radiative heat losses cause the local temperature to drop below a threshold temperature value, the freezing of soot burnout causes the emission of relatively cold soot downstream the flame as a smoking plume [13, 33, 34]. Large loads of glowing soot are reported at the smoke point transition [35], while no significant amount is observed near the flammability limit. As a consequence, soot-related observations are put forward in the following sections.

3. Experiments and diagnostics

The combustion chamber in which experiments are conducted is embedded into the Detection of Ignition And Mitigation Onboard for Non-Damaged

Spacecrafts (DIAMONDS) rig, extensively detailed in Refs. [5, 36]. DIAMONDS is flown aboard the Novespace A310 ZeroG airplane, which performs parabolic flights with repeated microgravity sequences of 22s and an accuracy level of $10^{-2}g_0$ (g_0=9.81 m.s^{-2}). Only key elements of the setup are briefly reminded here.

3.1. Flow conditions and flame configuration

In the 190 mm diameter combustion chamber, the laminar oxidizer flow is established with controlled oxygen content, pressure, and flow velocity. Oxygen content $x_{O_2,\infty}$ can be adjusted between 0 and 21% in volume, pressure levels P can range from 50 kPa to 150 kPa, and flow velocity u_∞ can be adjusted from 0 to 300 mm.s^{-1}. 150mm long cylindrical samples are located along the chamber axis. They consist of a 0.5 mm in diameter Nickel-Chrome metallic core coated by a 0.3 mm thick layer of LDPE and are mounted on sample holders. Every coating is ignited using a Kanthal wire. Once the steady rate propagation is achieved [37], measurements are conducted. Concurrent flow propagations investigated in this context could only reach a steady spread rate in low pressure, low oxygen content oxidizer flows, for which smoke emission was never reported. As such, concurrent spread data showed limited interest in the present study and only opposed-flow measurements are reported here.

3.2. Optical diagnostics

Images of the flame spread are captured using a JAI AT-140CL digital 12-bit tri-CCD camera, equipped with a telecentric lens. Light is collected by three 512×1396 pixels^2 CCD arrays over three spectral bands, ranging from

400nm to 510nm (blue), 480nm to 600nm (green), and 570nm to 700nm (red), respectively. The pixel resolution is 72.6 μm for each spectral band, and images are acquired at a rate of 39.06 fps. Behind the sample to be burnt, a white diffusive screen is illuminated by a set of adjustable RGBW LEDs which provide a uniform backlighting. This backlighting is alternatively set on and off throughout the parabola. When the backlight is on, smoking and non-smoking situations can be discriminated by examining the absorption fields throughout the plume. Subtracting successive frames with and without backlight gives access to the integrated absorption field in the flame, which provides soot volume fraction mappings in this configuration once the B-MAE technique is implemented [37, 38]. The B-MAE technique further provides temperature mappings in the soot-populated flame. In each flow situation investigated, camera and backlight parameters were adjusted to values prescribed for an optimal B-MAE post-processing [5]. This adjustable setting proved valuable to scale the dynamics of convoluted soot absorption and emission fields in flames which displayed a wide range of radiative intensities and optical thicknesses depending on the flow conditions.

4. Results and discussions

Figure 1 highlights the effect of flow conditions on smoke production, but does not provide insights regarding the mechanisms driving the observed transition. Capitalizing on results established in Part I [5], the influence of each parameter is analysed independently. It should be reminded that the results presented hereafter have been established over a specific narrow domain of flow conditions, intentionally selected for their proximity to standard breathable atmospheric conditions found on Earth.

4.1. Key results from Part I

Results detailed in the previous paper [5] can be summarized as follows: the spread rate, u_p, and, consequently, the pyrolysis mass flow rate, $\dot{m}_F$, are affected by flow conditions according to the following trends:

$$\dot{m}_F \;=\; C\;u_p \;=\; C\;(1+S)^{-1.06\;\pm\;0.73}\;u_\infty^{-0.12\;\pm\;0.13}\;P^{-0.09\;\pm\;0.14} \tag{1}$$

where the oxidizer/fuel mass ratio S is a decreasing function of the oxygen content $x_{O_2,\infty}$ and C a constant of normalization. Assuming the fuel is pure ethylene (see discussion in Section 4 of Ref. [5]), both quantities are related as follows:

$$1+S = 1+3\;\frac{32+28\;\frac{1\;-\;x_{O_2,\infty}}{x_{O_2,\infty}}}{28} \tag{2}$$

Considering that pyrolysis mass flow rate is marginally affected by both oxidizer flow velocity and pressure, the soot production residence time, $t_{res,s}$, is then featured in association with a characteristic soot production length L_s. This length is defined as the distance between the pyrolysis front, identified at the upstream front of the molten coating, and the position of the peak integrated soot volume fraction along the wire axis [37]. Soot volume fraction is provided by the B-MAE technique.

$$t_{res,s} \;=\; C\;\frac{L_s}{u_\infty} \;=\; C\;(1+S)^{-1.19\;\pm\;0.75}\;u_\infty^{-1.08\;\pm\;0.14}\;P^{-0.08\;\pm\;0.06} \tag{3}$$

Maximum soot volume fraction in the flame is also measured, and proved to be a function of all three flow parameters:

$$f_{s,max} \;=\; C\;(1+S)^{-9.3\;\pm\;1.95}\;u_\infty^{0.66\;\pm\;0.40}\;P^{2.96\;\pm\;0.29} \tag{4}$$

Given the independence of soot production residence time on pressure (see the exponent in Eq.(3)), the soot production reaction order in pressure was inferred from this peak soot volume fraction:

$$\dot{\omega}'''_{SP} \; = \; C \; P^{2.96 \, \pm \, 0.29} \tag{5}$$

4.2. Influence of oxygen content

The smoke point transition recorded as oxygen content varies is not a straightforward result. As oxygen content increases, two competing phenomena are recorded since both oxidation reactions and soot formation rates are increased. In order to identify the prevailing mechanisms over the range of oxygen contents of interest ($x_{O_2,\infty} \in [0.18; 0.21]$), the present experiment can be related to measurements conducted at normal gravity over an ethylene burner by Glassman and Yaccarino [10]. Looking at the influence of oxygen content in the oxidizing stream of a coflow diffusion flame at atmospheric pressure, they reported that within the range of oxygen contents considered in the present paper, increasing oxygen content primarily promotes soot oxidation rate in the flame. As such, starting with a smoking flame, the fuel flow rate had to be increased with oxygen content to maintain quenching conditions at the flame tip. Among other results, the authors reported the critical ethylene fuel flow rate at quenching $\dot{m}_F^c$ as a function of oxygen content. From the data they provided in the 18% - 21% oxygen content range, and plotting it in the $(1 + S, \, \dot{m}_F)$ frame, it appears that:

$$\dot{m}_F^c \; = \; C \; (1 + S)^{-0.82 \, \pm \, 0.14} \tag{6}$$

This evolution of the critical fuel mass flow rate can shed light on the present spreading flame configuration, as Eq. (6) is contrasted with the pyrolysis mass flow rate. Equation (1) shows that, as the flame spreads over the wire, the pyrolysis mass flow rate decreases with (1 + S) faster that the critical fuel mass flow rate reported in the experiments by Glassman and Yaccarino.

$$\dot{m}_F \;=\; C\;(1+S)^{-1.06\;\pm\;0.73} \tag{7}$$

Given the relation between (1 + S) and $x_{O_2,\infty}$, this means that, with respect to oxygen content, the pyrolysis mass flow rate in the present configuration increases faster than the critical mass flow rate required to sustain quenching conditions at the flame tip. At low oxygen content, the flame is non-smoking since the low spread rate generates a pyrolysis mass flow rate below the critical value at quenching. As oxygen content is increased, it is expected that the pyrolysis mass flow rate may exceed the critical value at quenching as a result of the sharp increase in spread rate. Thus, in the present situation, the transition from a non-smoking flame at low oxygen content to a smoking flame at high oxygen content is mainly interpreted as a consequence of the increase in spread rate.

4.3. Influence of pressure

Pressure marginally affects both flame spread rate and soot production residence time from $P = 70.9$ kPa to $P = 141.8$ kPa [5]. However, over this pressure range, the soot production rate in the present flames is approximately third-order in pressure (see Eq. (5)). Yet, soot-related radiative losses play a major role in the flame considered [37]. As pressure is increased, this surge in soot formation rate results in higher radiative losses in the flame which lower the local temperature and eventually quenches soot oxidation reactions at high pressure. This time, the transition from a non-smoking flame at low pressure levels to a smoking flame at high pressure levels is interpreted as a result of the increase in soot production rate.

4.4. Influence of flow velocity

Over the range of opposed flow velocities studied ($u_\infty \in$ [100 mm.s^{-1}; 200 mm.s^{-1}]), flow velocity marginally affects spread rate over the coated wire, but an increase in flow velocity raises the peak soot volume fraction while it curbs soot production residence time [5]. These two consequences have competing effects on soot-related radiative losses. From the results shown in Fig. 1, it should be noted that test conditions (P = 105 kPa, $x_{O_2,\infty}$ = 0.19), (P = 121 kPa, $x_{O_2,\infty}$ = 0.18), and (P = 141 kPa, $x_{O_2,\infty}$ = 0.17) repeated twice for each oxidizer flow velocity systematically revealed smoke in the flame plume at the highest flow velocity (200 mm.s^{-1}) but not at the lowest one (100 mm.s^{-1}). As such, the transition from a non-smoking to a smoking configuration can take place as flow velocity is increased, but this effect is minimal compared to the influence of oxygen content or pressure. Additional investigation at lower flow velocity could shed additional light on the influence of flow velocity. However, such low flow experiments require facilities providing a higher quality of microgravity [5].

4.5. Spacecraft atmosphere selection for increased fire safety

Based on the present set of data mapping the smoke point transition for thin flammable materials in opposed flow, and given the prominence of smoke-related incidents in space exploration, recommendation for atmospheric design would include reducing oxygen content and pressure. Indeed, the limited results presented here should be backed by additional smoke point investigations taking into account other materials and geometries to provide robust conclusions on the effect of ambient flow conditions on smoke emission.

From a fire safety perspective, this approach would have to be weighed against the impacts on flammability limit, ignitability, and flame spread rate. Experimental data on the flammability limit over the same configuration suggest that low pressure and low oxygen content also increase fire safety [31], as illustrated in Fig. 2. A similar trend is reported regarding the piloted ignition delay of thermally-thin cellulose in drop towers, showing that ignitability is inversely proportional to oxygen content and pressure, and independent of flow velocity [39]. However, results regarding the ignition delay time over PMMA slabs showed that, at higher flow velocity ($u_\infty >$ 400 mm.s^{-1}), ignitability increases as pressure is decreased due to the reduction in convective heat losses from the solid [40]. This latter statement calls again for a cautious interpretation of the results depending on the range of conditions studied. Given that flammability and ignitability have received more attention over the past decades, an extensive review of the literature to conclude on fire safety recommendations could be performed once more results on smoke point in a spreading situation are gathered.

Looking at the broader picture, spacecraft atmospheric design requires an optimal trade-off between material requirements and the scientific and technical specifications of the mission, within the range of atmospheric conditions the human body can adapt to without noticeable reduction in physical or intellectual performances [30]. The present situation in the International Space Station (P = 101.3 kPa, $x_{O_2,\infty}$ = 0.21) is a consequence of historic developments and scientific ambitions. Part of the originally planned elements of the ISS were inherited from the final version of the Mir-2 space station, which was designed with this conservative oxygen-nitrogen mixture at sea level pressure [41]. Incidentally, this environment is ideal to single out the impact of weightlessness on the human body, which benefited the numerous medical studies performed over the past 20 years. Yet, this high pressure means that a pre-breathing period of about two hours is required prior to any extra-vehicular activity (EVA) to avoid decompression sickness when donning the low pressure space suit [42]. In the context of exploration missions, a design risk analysis should help find an optimal pressure low enough to support short EVA pre-breathing time, reduced structural weight, and increased fire safety, but high enough to avoid a sudden lethal depressurization in case of leakage.

As stated in the introduction, the normoxic curve has been regularly put forward as a solution to benefit from low pressure conditions while keeping oxygen partial pressure constant. But from a fire safety perspective, the rise in oxygen content as pressure is decreased can nullify the benefits of low pressure environments. For instance, Fig. 1 shows that the normoxic curve crosses the smoke point boundary, meaning that smoke-related danger is increased at low pressure normoxic conditions. Because the human body can adapt to low pressure / low oxygen content atmospheric conditions, the potential for exploration atmosphere below the normoxic curve should be studied closely. As an illustration, conditions at $P = 70$ kPa and $x_{O_2,\infty} = 0.21$ increase fire safety as compared to present ISS conditions while staying away from the minimum breathing conditions with acclimatization. Starting from this set of ambient conditions, the consequences on fire safety of an increase in oxygen content conjoint to a decrease in pressure in order to allow efficient EVA preparation should be carefully considered.

It should be pointed out that the results of past risk-based systems engineering analyses for spacecraft, which did not consider past smoke release incidents, were detrimental to fire risk concerns (see Table 4 of [43]). Prioritizing strict hypoxia standards and mission operation requirements, exploration atmospheres with oxygen contents over 30% were recommended. Yet, above this threshold, standard material flammability control methods such as fluoropolymer coating may no longer work on off-the-shelf equipment items.

4.6. Temperature at quenching

As an outcome related to the smoke point transition, the temperature of soot particles in smoking flames has been investigated to identify a characteristic level for the extinction, or quenching, of soot oxidation reactions. Since the B-MAE technique provides soot volume fraction and temperature fields, such temperature can be found as the threshold at which soot oxidation reactions are frozen in the flame.

Similar measurements have been already performed over different burner configurations, providing clues regarding the transition from non-smoking to smoking flames. Ground-based experiments by Kent and Wagner [12, 44], or more recently by Bonnety et al. [34] reported local soot oxidation reaction extinction temperatures of 1300-1500 K in flames established over burners at normal gravity. Kent and Wagner measured soot temperature using the optical Kurlbaum method, in which the line of sight average soot temperature is weighted to regions of high soot volume fraction. Identifying the plateau of integrated soot volume fraction $F_s(z) = \int_0^\infty 2\pi r f_s(r,z) dr$, they showed that unoxidized soot particle escape the flame tip as local temperature drops to a 1300-1400 K threshold for methane, acetylene, ethylene, propane, and butane flames. With a different optical setup, Bonnety et al. [34] implemented the spectral MAE technique over ethylene flames to map soot volume fraction and temperature, and reached a comparable temperature threshold of 1400-1500 K.

Similar measurements were performed in microgravity over ethylene flames by Urban et al. [45] and Diez et al. [46]. However, these studies did not determine a characteristic temperature for soot oxidation reaction extinction. Urban et al. [45] found local soot temperature of about 1000 K at the luminous flame tip of smoking flames, after mapping soot temperature distributions using a deconvoluted absorption and emission technique which ignored soot self-absorption. As cold soot particles escaped from the flame tip, they could conclude on the presence of extinction mechanisms. Yet they did not conduct a similar integrated volume fraction analysis to identify a quenching location. Mapping temperature at the tip of non-smoking flames, Diez et al. [46] identified temperatures ranging from 1750 K to 1400 K as the conditions reached local extinction. In order to justify the universality of the lower temperature value they measured as a soot quenching temperature, a systematic observation of local extinction was conducted with a methodology similar to that followed on ground-based experiments.

The similarities between the MAE optical setup by Bonnety et al. [34] and the B-MAE presently employed stress that flame properties such as soot self-absorption are handled alike. In addition, the same definition of quenching location as the position along the streamwise coordinate z where the integrated soot volume fraction reaches a plateau is adopted. Figure 3 highlights the temperature measurement process for a given set of flow conditions at which quenching occurs. The volume fraction mapped on the left is integrated radially, and F_s is plotted as function of the streamwise coordinate in the central plot. The location of the plateau is extracted, with an approximation of $\pm$ 0.36 mm (5 pixels) to account for geometric approximation and increased uncertainty in the soot model adopted in the deconvolution as soot particles may increase in size. The temperature mapped on the right is then averaged at the location of interest, using the radial soot volume fraction distribution as a weight distribution. In this case, a f_s-weighted quenching temperature of 1401 K $\pm$ 11 K can be identified.

Reporting this temperature of extinction in various quenching conditions, Fig. 4 illustrates the effect of pressure at different flow velocities, while keeping oxygen content, and consequently spread rate, constant. Recalling the uncertainty of $\pm$ 50 K in temperature measurements from the B-MAE technique, the extinction temperature is not affected by pressure or flow velocity. A mean value of about 1400 K can be extracted from this graph.

Investigating then the effect of oxygen content variations, Fig. 5 reports similar results and confirms the quenching temperature of 1400 K at various pressure and oxygen contents, with a set flow velocity. While these results agree with those provided by Kent and Wagner [12, 44], Bonnety et al. [34], and Diez et al. [46], they provide higher temperature than that reported by Urban et al. [45], well above the uncertainty level.

Four differences in the two sets of measurements performed in microgravity could explain the temperature discrepancy. First, Urban et al. [45] conducted microgravity measurements in a Space Shuttle, while the present results are obtained in parabolic flights. Looking at other flame characteristics, Urban et al. noticed how long-duration combustion experiments show different results from those obtained in ground-based microgravity facilities. Second, two different definitions of the streamwise location of interest for temperature measurement are adopted. The location of the luminous flame tip captured by the optical setup, used by Urban et al., is dictated by the visible intensity, i.e. mainly by both soot volume fraction and temperature fields, while the soot plateau analysis relies only on soot volume fraction measurements. From the present set of data, the luminous flame tip is reported to occur downstream of the soot plateau for all the conditions shown in Figs. 4-5, meaning that the temperature at the flame tip is lower than that at the soot plateau. As an illustration, the luminous tip of the flame displayed in Fig. 3 would be located at $z = 22.0$ mm ± 0.2 mm, downstream of the soot plateau identified at $z_{ox} = 19.3$ mm ± 0.4 mm. Third, as the post-processing of the diagnostics deployed by Urban et al. ignores reabsorption, soot temperature measurements are likely to be underestimated. However, the resulting discrepancy is expected to be an order of magnitude lower that the 400 K of difference seen here [35]. Last, the opposed flow configuration can favour early smoke point transition in a way that is different from the laminar jet flames. Since the NiCr metallic core crosses the flame front, heat losses through solid conduction and surface radiations keep the core temperature below that of the flame. As such, local quenching of oxidative reactions in the vicinity of the axis is expected for all flow conditions. If the temperature of soot oxidation freezing is universal, it should be independent of this consideration. However, should the location of the soot plateau be moved upstream due to accumulation of cold soot near the axis, then higher temperature for soot oxidation could be reported. The latter effect is however considered negligible, since most of the soot is located away from the axis in the present configuration (see Fig. 3).

5. Conclusion

Oxygen content and pressure play a major role in smoke production of flames spreading over solid samples, while flow velocity marginally affects the transition from non-smoking to smoking flames in the range of conditions considered. Capitalizing on results from the previous paper and isolating each parameter, potential mechanisms explaining the observed smoke point transition are proposed. An increase in oxygen content, all other flow parameters being constant, increases the spread rate and thus pyrolysis rate, triggering the transition from non-smoking to smoking flame. The same transition when pressure is increased is caused by the cubic dependency of soot formation rate with pressure. In both situations, the increased soot load boosts soot radiative losses, dropping local temperature to a level such that soot oxidation reactions are frozen. Identifying the location at which soot reaction quenching occurs and reporting the local temperature for a relatively broad range of flow conditions, a threshold of 1400 K is identified, comforting both observations previously made at normal gravity and insights from earlier microgravity experiments. This first systematic characterisation of the role of flow conditions on smoke emission for a flame spreading over a solid sample should be followed by similar investigations with different material and geometries to extend the present results. Contrasting fire safety concerns with other atmospheric considerations for spacecraft design, the present study tends to support the implementation of low pressure and low oxygen content below the normoxic curve to mitigate smoke emission.

Acknowledgments

The authors feel grateful to the Centre National d'Etudes Spatiales (CNES) for its financial support under Contract No. 130615.

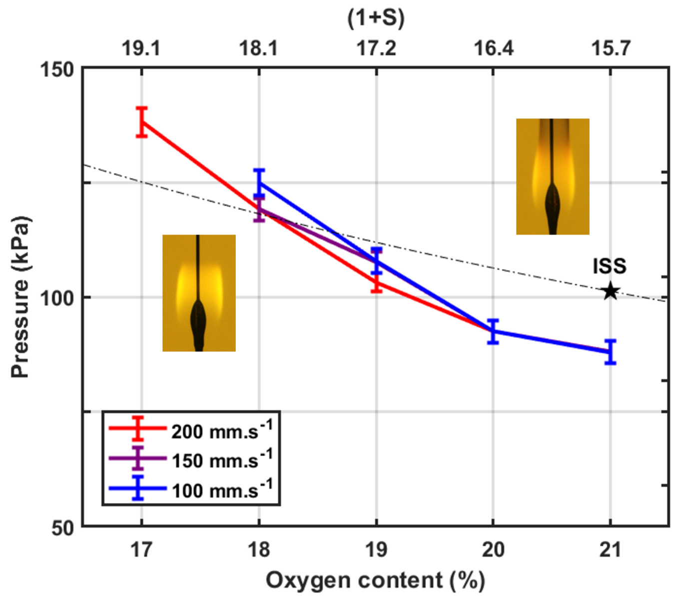

Figure 1: Effects of pressure and oxygen content on the transition between non-smoking and smoking flames, for three different opposed-flow velocities. The smoke point transition occurs as pressure or oxygen content is increased, almost independently of flow velocity. The normoxic curve is reported as a dotted line, and a star indicates nominal atmospheric conditions (P = 101.3 kPa, $x_{O_2,\infty}$= 0.21) used in the International Space Station (ISS).

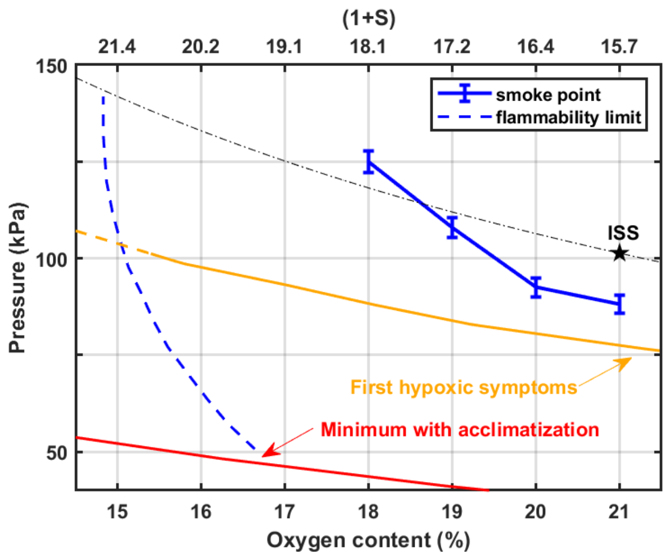

Figure 2: Pressure at smoke point transition and flammability limit [31] as a function of oxygen content. The normoxic curve is reported as a black dotted line, and a star indicates the atmospheric conditions used in the ISS. Atmospheric conditions above the orange line are fit to normal human breathing, and the human body can adapt to conditions down to the red line (extracted from Tobias [29]).

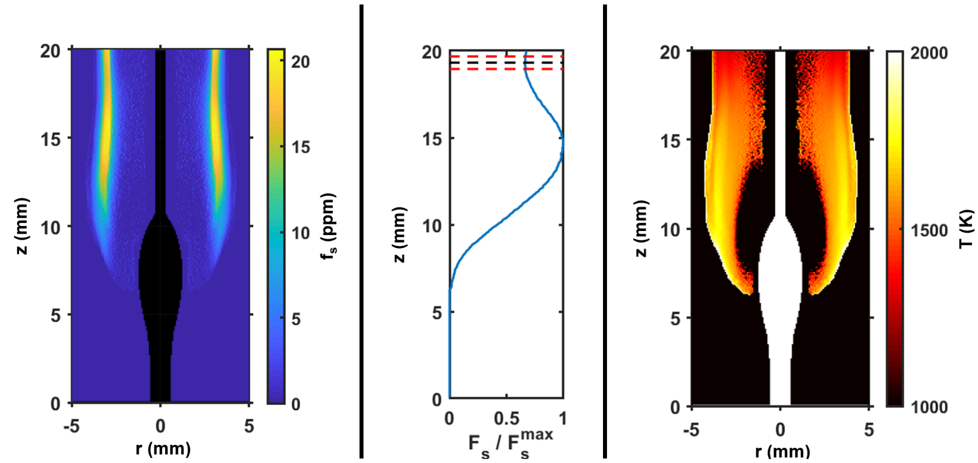

Figure 3: Procedure to determine quenching location and temperature in a smoking flame, u_∞ = 150 mm.s^{-1}, $x_{O_2,\infty}$ = 0.19, and P = 131 kPa. (a) Soot volume fraction mapping shows the release of cold soot particles, while (b) the evolution with the streamwise coordinate z of the radially integrated soot volume fraction F_s ends with a plateau, identifying a location beyond which soot oxidation reactions are frozen z_{ox} = 19.3 mm ± 0.4 mm. (c) Temperature mappings eventually provide the corresponding quenching conditions.

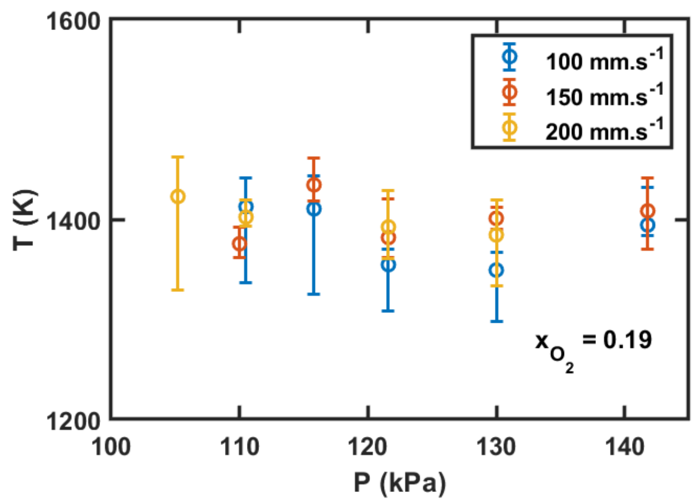

Figure 4: Quenching temperature as a function of pressure for different flow velocities, at an oxygen content $x_{O_2,\infty} = 0.19$. Data at low pressure are only reported in quenching situations. A mean value of 1395 K $\pm$ 25 K can be extracted from this graph.

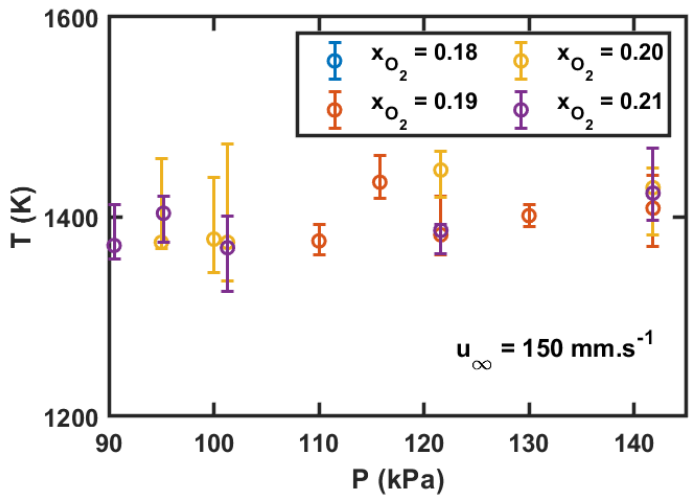

Figure 5: Quenching temperature as a function of pressure for different oxygen contents, at a flow velocity $u_\infty = 150$ mm.s^{-1}. Data at low pressure are only reported in quenching situations. A mean value of 1399 K $\pm$ 25 K can be extracted from this graph.

[1] J. Crusan, Habitation module, NASA Advisory Council, Human Expl. Op. Committee (2016).

[2] C. Harrison, S. Weaver, C. Bertelsen, E. Burgett, N. Hertel, E. Grulke, Polyethylene/boron nitride composites for space radiation shielding, J. App. Polymer Sci. 109 (2008), 2529–2538.

[3] J. Graf, C. Dunlap, J. Haas, M. Weislogel, J. Lewis, K. Meyers, A. McKernan, Development of a solid chlorate backup oxygen delivery system for the International Space Station, SAE Technical Paper No. 2000-01-2348 (2000).

[4] G. E. Apostolakis, I. Catton, T. Paulos, K. Paxton, S. Jones, Findings of a review of spacecraft fire safety needs, NASA Technical Reports 19930004527 (1992).

[5] A. Guibaud, J.M. Citerne, J.L. Consalvi, G. Legros, On the effects of opposed flow conditions on non-buoyant flames spreading over polyethylene-coated wires - Part I: spread rate and soot production, Combust. Flame (2020), Accepted for publication.

[6] A. A. Siddiqi, Challenge to Apollo: the Soviet Union and the space race, 1945-1974, NASA History Series (2000).

[7] J.E. Oberg, Star-crossed orbits: inside the US-Russian space alliance, McGraw-Hill Companies (2002).

[8] Standard test method for density of smoke from the burning or decomposition of plastics, ASTM D2843 (2004).

[9] R.A. Hunt, Relation of smoke point to molecular structure, Ind. Eng. Chem. 45 (1953), 602–606.

[10] I. Glassman, P. Yaccarino, The effect of oxygen concentration on sooting diffusion flames, Comb. Sci. Technol. 24 (1980), 107–114.

[11] K.P. Schug, M.T. Yaccarino, P. Yaccarino, I. Glassman, Sooting behavior of gaseous hydrocarbon diffusion flames and the influence of additives, Comb. Sci. Technol. 22 (1980), 235–250.

[12] J.H. Kent, H.Gg. Wagner, Why do diffusion flames emit smoke?, Comb. Sci. Technol. 41 (1984), 245–269.

[13] G.H. Markstein, J. De Ris, Radiant emission and absorption by laminar ethylene and propylene diffusion flame, Proc. Comb. Inst. 20 (1984), 1637–1646.

[14] W.L. Flower, C.T. Bowman, Soot production in axisymmetric laminar diffusion flames at pressures from one to ten atmospheres, Symp. Int. Comb. 21 (1988), 1115–1124.

[15] T.L. Berry, W.L. Roberts, Measurement of smoke point in velocity-matched coflow laminar diffusion flames with pure fuels at elevated pressures, Comb. Flame 145 (2006), 571-578.

[16] T.L. B. Yelverton, W.L. Roberts, Effect of dilution, pressure, and velocity on smoke point in laminar jet flames, Comb. Sci. Technol. 180 (2008) 1334–1346.

[17] H. Li, H. Yaping, W. Jian, Determination of smoke point of laminar acetylene diffusion flames under subatmospheric pressures, Comb. Sci. Technol. 186 (2014), 1237-1248.

[18] P.B. Sunderland, S. Mortazavi, G.M. Faeth, D.L. Urban, Laminar smoke points of nonbuoyant jet diffusion flames, Comb. Flame 96 (1994), 97–103.

[19] D. Urban, Z.G. Yuan, P.B. Sunderland, K.C. Lin, Z. Dai, G.M. Faeth, Smoke-point properties of non-buoyant round laminar jet diffusion flames, Proc. Comb. Inst. (2000), 1965–1972.

[20] D. Urban, D. Griffin, G. Ruff, T. Cleary, J. Yang, G. Mulholland, Z.G. Yuan, Detection of smoke from microgravity fires, SAE Transactions (2005), 375–384.

[21] M. Kikuchi, O. Fujita, K. Ito, A. Sato, T. Sakuraya, Experimental study on flame spread over wire insulation in microgravity, Symp. Int. Comb. 27 (1998), 2507–2514.

[22] S.L. Olson, F.J. Miller, Experimental comparison of opposed and concurrent flame spread in a forced convective microgravity environment, Proc. Comb. Inst. 32 (2009), 2445–2452.

[23] L.G. Moore, Measuring high-altitude adaptation, J. App. Physiol. 123 (2017), 1371–1385.

[24] E.A. Koller, M. Bischoff, A. Bührer, L. Felder, M. Schopen, Respiratory, circulatory and neuropsychological responses to acute hypoxia in

acclimatized and non-acclimatized subjects, Europ. J. app. phys. occup. phys. 62 (1991), 67–72.

[25] E. Stauffer, E. Loyrion, I. Hancco, X. Waltz, M. UllielRoche, L. Oberholzer, P. Robach, A. Pichon, J.V. Brugniaux, P. Bouzat, S. Doutreleau, P. Connes, S. Verges, Blood viscosity and its determinants in the highest city in the world, J. Physiol. Accepted for publication (2020).

[26] P. Brimblecombe, Air composition and chemistry, Cambridge University Press (1996).

[27] H.L. Hartman, J.M. Mutmansky, R.V. Ramani, Y.J. Wang, Mine ventilation and air conditioning, John Wiley & Sons (2012).

[28] J.H. Comroe, R.D. Dripps, P.R. Dumke, M. Deming, Oxygen toxicity: the effect of inhalation of high concentrations of oxygen for twenty-four hours on normal men at sea level and at a simulated altitude of 18,000 feet, J. Am. Med. Assoc. (1945), 710–717.

[29] L. Tobias, Apollo applications program payload integration technical study and analysis report, Bendix Corp. technical report (1967).

[30] K.E. Lange, A.T. Perka, B.E. Duffield, F.F. Jeng, Bounding the spacecraft atmosphere design space for future exploration missions, NASA Technical Reports 20050185597 (2005).

[31] M. Nagachi, J.-M. Citerne, H. Dutilleul, A. Guibaud, G. Jomaas, G. Legros, N. Hashimoto, O. Fujita, Effect of ambient pressure on the extinction limit for opposed flame spread over an electrical wire in microgravity, Proc. Combust. Inst. 38 (2020), Accepted for publication.

[32] S.L. Olson, P.V. Ferkul, J.S. Tien, Near-limit flame spread over a thin solid fuel in microgravity, Symp. Int. Combust. 22 (1989), 1213–1222.

[33] J.H. Kent, A quantitative relationship between soot yield and smoke point measurements, Combust. Flame 63 (1986, 349–358.

[34] J. Bonnety, A. Guibaud, R. Jalain, A. Matynia, J.-L. Consalvi, F. Liu, G. Legros, Probing the local radiative quenching during the transition from a non-smoking to a smoking laminar coflow ethylene/air non-premixed flame, Comb. Flame 203 (2019), 120–129.

[35] A. Guibaud, J.-M. Citerne, J.-L. Consalvi, J.L. Torero, O. Fujita, M. Kikuchi, P. Ferkul, N. Smirnov, G. Jomaas, B. Toth, S. Rouvreau, G. Legros, Accessing the soot-related radiative heat feedback in a flame spreading in microgravity: optical designs and associated limitations, Proc. Combust. Inst. 38 (2020), Accepted for publication.

[36] J.M. Citerne, H. Dutilleul, K. Kizawa, M. Nagachi, O. Fujita, M. Kikuchi, G. Jomaas, S. Rouvreau, J.L. Torero, G. Legros, Fire safety in space - investigating flame spread interaction over wires, Acta Astronautica 126 (2016), 500–509.

[37] A. Guibaud, J.M. Citerne, J.L. Consalvi, O. Fujita, J.L. Torero, G. Legros, Experimental evaluation of flame radiative feedback: methodology and application to opposed flame spread over coated wires in microgravity, Fire Tech. 56 (2020), 185–207.

[38] A. Guibaud, J.M. Citerne, J.M. Orlac'h, O. Fujita, J.L. Consalvi, J.L. Torero, G. Legros, Broadband modulated absorption/emission tech-

nique to probe sooting flames: Implementation, validation, and limitations, Proc. Comb. Inst. 37 (2019), 3959–3966.

[39] S.L. Olson, Piloted ignition delay times of opposed and concurrent flame spread over a thermally-thin fuel in a forced convective microgravity environment, Proc. Combust. Inst. 33 (2011), 2633-2639.

[40] S. McAllister, C. Fernandez-Pello, D. Urban, G. Ruff, Piloted ignition delay of PMMA in space exploration atmospheres, Proc. Combust. Inst. 32 (2009), 2453-2459.

[41] E.M. Roth, Space cabin atmospheres, NASA Technical Reports N64-30345(1964).

[42] K.B. McCarthy, J.A. Green, The effect of reduced cabin pressure on the crew and the life support system, SAE Transactions (1991), 646–650.

[43] NASA Exploration Atmospheres Working Group, Recommendations for exploration spacecraft internal atmospheres - the final report of the NASA Exploration Atmospheres Working Group (EAWG), NASA TP-2010-216134 (2006).

[44] J.H. Kent, H.Gg. Wagner, Temperature and fuel effects in sooting diffusion flames, Symp. Int. Comb. 20 (1985), 1007–1015.

[45] D.L. Urban, Z.G. Yuan, P.B. Sunderland, G.T. Linteris, J.E. Voss, K.C. Lin, Z. Dai, K. Sun, G.M. Faeth, Structure and soot properties of nonbuoyant ethylene/air laminar jet diffusion flames, AIAA journal 36 (1998), 1347–1360.

[46] F.J. Diez, C. Aalburg, P.B. Sunderland, D.L. Urban, Z.G. Yuan, G.M. Faeth, Soot properties of laminar jet diffusion flames in microgravity, Comb. Flame 156 (2009), 1514–1524.